Atomic-layer synthesis and imaging uncover broken inversion symmetry in La_{2−x}Sr_{x}CuO_{4} films

Yizhak Yacoby, Hua Zhou, Ron Pindak, and Ivan Božović

Phys. Rev. B **87**, 014108 — Published 22 January 2013

DOI: 10.1103/PhysRevB.87.014108

Atomic-layer synthesis and imaging uncover broken inversion symmetry in $La_{2-x}Sr_xCuO_4$ films

Yizhak Yacoby[1], Hua Zhou[2], Ron Pindak[3*] and Ivan Božović[4]

[1] Racah Institute of Physics, Hebrew University, Jerusalem 91904, Israel

[2] Advanced Photon Source, Argonne National Laboratory, Argonne, Illinois 60439, U.S.A.

[3] Photon Sciences Directorate, Brookhaven National Laboratory, Upton, New York 11973, U.S.A.

[4] Condensed Matter Physics & Materials Science Department, Brookhaven National Laboratory, Upton, New York 11973, U.S.A.

PACS number: 74.72.-h, 74.78.-w, 61.05.cf, 81.15.Aa, 61.50.Ah, 11.30.Qc

Abstract

Materials with broken inversion symmetry are of great interest for their exotic electronic properties, but are relatively rare. We show here that even if a material is inversion-symmetric in the bulk form, in epitaxial thin films of the same compound the crystallographic unit cell can be quite asymmetric. To demonstrate this, we have used atomic-layer-by-layer molecular beam epitaxy (ALL-MBE) to synthesize $La_{2-x}Sr_xCuO_4$ films with Sr dopant atoms deposited above, below, or on both sides of each CuO_2 layer. Surface X-ray diffraction experiments analyzed by the Coherent Bragg Rod Analysis (COBRA) method have been carried out in combination with energy-differential diffraction measurements to determine whether the actual Sr distribution coincided or not with the nominal one (that would be expected in absence of La-Sr interdiffusion). The differential approach minimizes the systematic errors and the combination with COBRA is potentially capable to determine the concentration of atomic species on a mono-atomic layer-by-layer basis. The results show that the concentration of Sr in La/Sr layers just above the CuO_2 layers is much larger than in layers just below them, irrespective of the deposition sequence, and drastically breaking the inversion symmetry.

I. INTRODUCTION

In crystals with broken inversion or mirror symmetry, certain uncommon material's properties can attain non-zero values, giving rise to some of the most interesting electronic phenomena. Examples include spontaneous polarization giving rise to ferroelectricity [1], toroidal moment in multiferroics [2-4], Rashba spin-orbit coupling giving rise to triplet superconductivity [5] and time-reversal symmetry breaking in topological insulators [6]. However, strongly broken inversion symmetry occurs relatively rarely in bulk crystals, and not always in conjunction with other desired (electrical, magnetic, mechanical, etc.) material properties. Here, we report a strong spontaneous breakdown of inversion symmetry in thin epitaxial films of compounds that in bulk form are symmetric. This is demonstrated using as an example a high-temperature superconductor $La_{1-x}Sr_xCuO_4$ (LSCO). Characterizing and understanding this phenomenon may lead to the development of a method to synthesize thin films of materials with new and interesting combination of properties.

The present discovery originated from a systematic study of interface superconductivity that occurs in metal-insulator (*M-I*) bilayers where *M* = $La_{1.55}Sr_{0.45}CuO_4$, a non-superconducting metal, and *I* = La_2CuO_4, an antiferromagnetic insulator [7-9]. The key question here is whether this interface superconductivity is primarily an electronic or a chemical phenomenon, i.e., whether its origin is in the charge transfer (electron accumulation and depletion) across the interface or it is just a result of inadvertent chemical doping due to e.g., Sr diffusion from $La_{1.55}Sr_{0.45}CuO_4$ into La_2CuO_4. The same question is also encountered in the study of interfaces

in other important oxide bilayer heterostructures such as $LaAlO_3/SrTiO_3$, $LaAlO_3/LaNiO_3$, $YBa_2Cu_3O_7/La_{0.67}Sr_{0.33}MnO_3$, etc [10-13].

We applied the Coherent Bragg Rod Analysis (COBRA) phase-retrieval X-ray diffraction technique to study this question, and found that inter-diffusion was significant but restricted to an interface layer only 1-2 unit cells thick. This conclusion has been corroborated by other techniques (transmission electron microscopy, time-of-flight ion scattering and recoil spectroscopy, resonant soft x-ray scattering) [7, 14] as well. COBRA analysis also uncovered a new result that the Sr distribution appeared to be asymmetric: the concentration of Sr in adjacent La/Sr layers seemed to alternate so that adjacent layers had significantly different Sr concentrations. This result was unexpected and it's defying the broadly accepted tenet that if two different atomic species can occupy the same lattice site, the probability of one species occupying the site should be equal to its relative concentration.

However, since Sr concentration in the films we studied is relatively low and the number of electrons in La is only 1.5 times larger than in Sr, the scattering contrast is weak. For these reasons, the effect we observed was at the limit of our experimental resolution and barely measurable. To draw an unambiguous conclusion, it was necessary (i) to significantly improve the sensitivity of the technique and (ii) to custom-design heterostructure films in a way that would maximize the effects of growth dynamics on the Sr concentration distribution. Both goals have been achieved and are reported here.

We used atomic-layer-by-layer molecular beam epitaxy (ALL-MBE) [7-9, 15] to synthesize multilayer LSCO films. The growth sequences were varied to deposit Sr at different positions. The local Sr concentration was determined by a new differential method, which requires measuring the diffraction intensities at each point along the [00L] Bragg rod at two different X-ray photon energies. We demonstrate that regardless of how Sr is supplied most LSCO layers show dramatic asymmetry of the unit cell. Independent of whether Sr was deposited before or after Cu, we see very little or no Sr below the CuO_2 planes and a large Sr concentration above. A strong breakdown of inversion symmetry is confirmed in thin epitaxial films of La-based cuprate compounds that in bulk form are symmetric.

II EXPERIMENTAL METHODS

a. MBE synthesis

The films for this study were synthesized in a unique molecular beam epitaxy (MBE) system designed for atomic layer engineering of complex oxide materials [15]. The films were deposited at T = 650ºC and under p = 9×10^{-6} Torr of ozone. We used $10\times10\times1$ mm^3 single-crystal $LaSrAlO_4$ (LSAO) substrates polished perpendicular to the (001) crystal axis. The LSAO lattice constants are $a_0 = b_0 = 3.755$ Å and $c_0 = 12.636$ Å. The films are pseudomorphic with LSAO and under compressive strain. They were characterized in real time by reflection high-energy electron diffraction (RHEED) and subsequently by X-ray diffraction, atomic force microscopy (AFM), and measurements of magnetic susceptibility by the mutual inductance technique. The root-mean-square (rms) surface roughness as determined by AFM scans over a large (100 μm^2) area was 0.2 - 0.5 nm, significantly less than the unit cell height. The atomic

scale smoothness and high quality of cuprate heterostructures grown by this equipment have been amply illustrated before, including a demonstration of interface superconductivity in *M-I* bilayers [7] with a high-temperature superconductivity in a single CuO_2 layer [8, 9].

In this paper, we show the COBRA results for three films, each of which was 6 unit cells thick, which corresponds to 12 LSCO formula units. (The unit cell is doubled by a glide plane and contains two formula units.)

Sample S1 was an *M-I* bilayer, with 6 layers of *M* and 6 layers of *I*. While the constituent materials are not superconducting per se, the bilayer shows interface superconductivity. The measured critical temperature in this sample was T_c = 35 K, with a very sharp (< 1K) transition. The shuttering (deposition) sequence in these films was as follows: in the *M* part, La and Sr source shutters were opened simultaneously to deposit $La_{1.55}Sr_{0.45}O_2$, i.e., the total of two (La,Sr)O layers. (The La and Sr fluxes were not perfectly matched and the Sr shutters closed a little ahead of La shutters.) Then we deposited one CuO_2 layer. This was repeated six times, see Fig. 1a. Then, in the *I* part, analogously we first deposited two LaO layers, then a single CuO layer, again repeating this six times. In our extensive experience (over 1,800 LSCO growth experiments) this growth recipe provides the desired "214" crystal structure; the small Cu^{2+} cations 'sink' and find their right place. Indeed, in this manner we have grown hundreds of atomically perfect LSCO films with sharp superconducting transitions, as well as hundreds of heterostructures, multilayers and superlattices, with single-atomic-layer precision [7-9, 14, 15].

Sample S2 was a pure *M* film, 12 layers of $La_{1.56}Sr_{0.44}CuO_4$. In this case, the deposition was atomic-layer-by-layer. We first deposited a single $La_{0.56}Sr_{0.44}O$ layer, followed by CuO_2 and then by a LaO layer. In this way, the entire Sr doping was unloaded in the atomic layer immediately *below* the CuO_2 layer, see Fig. 1b. ('below' here means closer to the substrate.)

Sample S3 was also a pure *M* film, 12 layers of exactly the same $La_{1.56}Sr_{0.44}CuO_4$ composition. However, the deposition sequence was reversed: we first deposited a single LaO layer, followed by CuO_2 and then by a $La_{0.56}Sr_{0.44}O$ layer. The entire Sr doping was now unloaded immediately *above* the CuO_2 layer, see Fig. 1c.

b. Differential COBRA method

In ultrathin films, like the ones discussed here, some layers may not have full occupancy. Thus, in order to determine the layer-by-layer content of a chemical species, it is necessary to use its scattering cross-section energy dependence [16]. The problem is that the overall change in the diffraction intensity resulting from the change in X-ray photon energy is in the present case quite small. Let us consider for example two extreme cases: (a) a single monolayer containing only La, and (b) a monolayer consisting of 55% La and 45% Sr (twice the average nominal Sr concentration). The difference in scattering cross section of Sr measured just below the absorption edge, where it has a minimum, and 0.5 keV below it, is 6 electrons. Of course, if the layer contains no Sr, as in our case (a), the scattering cross-section in the vicinity of the Sr absorption edge will be independent of energy. Hence, the absolute difference in the average scattering cross-section of the layers (a) and (b) would be only 2.7 electrons, which amounts to

about 6%. So even between these two extreme cases the change would be very small, thus necessitating a highly accurate measurement.

The main sources of error in measuring the diffraction intensities are systematic, coming from uncertainties in the background subtraction and from errors in determining the position along the Bragg rod and the diffraction phases. If the entire data set is measured and analyzed at each energy and only the final results compared, these errors are largely independent and add [16]. On the other hand, if the diffraction intensity is measured differentially, i.e., if one measures the *difference* in the diffraction intensities at the two energies at each point along the Bragg rod, the errors partially cancel.

A method to determine the electron density (EDY) and the atomic species at the interface of a single crystal and an aqueous solution was presented by Park and Fenter [17]. This method derives the atomic structure by measuring the diffraction intensity as a function of energy in the vicinity of the absorption edge of the atomic species of interest at a number of points along the specular reflection truncation rod. Cation distribution in the aqueous phase near the interface can be determined robustly in a model-independent fashion. To the best of our knowledge, however, this resonant-anomalous-type method has not been applied to any complex epitaxial thin films, mainly because measuring the full energy spectrum at a number of points along the truncation rods is very time consuming. In principle the new method presented here, enables one to determine the layer by layer concentration by using the COBRA technique in combination with the measurement of the difference in diffraction intensities at just 2 energies.

In general, the differential COBRA procedure begins with measurement of the diffraction intensities along all the symmetry nonequivalent Bragg rods at an energy lower and far away from the absorption edge of the atomic species of interest. This constitutes a complete COBRA data set. Then the differential diffraction intensity is measured along the Bragg rods. At each point along the rod the difference between the diffraction intensities at two X-ray photon energies one just below the absorption edge and the other far below it are measured making sure that each difference is measured at exactly the same point along the rod. To analyze the data and determine the concentration of a chosen atomic species it is necessary to know its cross section at the two energies used. The scattering cross-section at the lower energy is taken from tables of X-ray atomic scattering factors. At energies close to the absorption edge the cross-section depends on the environment of the probe atom and needs to be determined experimentally. This is done using the Diffraction Anomalous Fine Structure (DAFS) method [18] as described in the following sub-section.

Using COBRA [19] and the Difference map method [20] the effective EDY is then determined from the full data set measured at the lower energy. At each site i the effective EDY $\rho_i(\vec{r}-\vec{r}_i)$ is normalized so that

$$\int \rho_{ij}(\vec{r}-\vec{r}_i)d^3r = f_{oj} + f'_{Aj} \qquad (1)$$

Here f_{0j} and f'_{Aj} are the ordinary and the real anomalous scattering factors of atom type j at site i. $\rho_{ij}(\vec{r}-\vec{r}_i)$ can now be divided into two components:

$$\rho_{ij}(\vec{r}-\vec{r}_i) = \rho^o_{ij}(\vec{r}-\vec{r}_i)f_{oj} + \rho^A_{ij}(\vec{r}-\vec{r}_i)f'_{Aj} \qquad (2)$$

and ρ^o, ρ^a, are normalized so their volume integrals around the site are equal to unity:

$$\int \rho^o d^3r = \int \rho^A d^3r = 1 \tag{3}$$

We assume that if more than one atom occupies the same site the EDY distributions are the same up to the normalization constant.

Both EDY distributions ρ^o and ρ^A are the result of folding the structure into one 2D unit cell. The folded structure is obtained by translating each atom to one substrate defined 2D unit cell using substrate defined 2D unit cell vectors and taking into account thermal vibrations. [21] By definition the anomalous contribution is k - independent and is therefore obtained by folding the structure with the electrons in each atom located at its center while ρ^o is obtained by folding the atoms taking into account the electron distribution in the atoms.

The two distributions are therefore related to each other. ρ^o is obtained by convoluting ρ^A with the electron distribution of a single atom.

$$\hat{\rho}^o = \hat{\rho}^A \Phi(k) \tag{4}$$

Here, $\hat{\rho}$ is the Fourier transform of ρ; $\Phi(k)$ is the 3D atomic form factor [22] normalized to unity at $\vec{k} = 0$. Notice that Eq. 4 preserves the normalization of ρ^o.

We can now express $\hat{\rho}^o$ and $\hat{\rho}^A$ in terms of $\hat{\rho}$.

$$\hat{\rho}^A = \frac{\hat{\rho}}{f_A^r + f_o \Phi(\vec{k})} \tag{5}$$

$$\hat{\rho}^o = \frac{\hat{\rho}\Phi(\vec{k})}{f_A^r + f_o \Phi(\vec{k})} \tag{6}$$

The overall EDY at the lower photon energy can now be expressed in the form:

$$\rho_L = \sum_{i,j} \rho_{ij}(\vec{r} - \vec{r}_i) c_{ij} \tag{7}$$

Here c_{ij} represents the fractional occupancy of site i by atom type j. The diffraction intensity

$$I_L(\vec{k}) = D(\rho_L, \vec{k}) \tag{8}$$

where D is the operator converting the EDY to the diffraction intensity at point $\vec{k}$ along the Bragg rod.

The effective EDY at the higher energy is given by

$$\rho_H = \rho_L + \sum_i \rho_{i1}^A(\vec{r} - \vec{r}_i) c_{i1} \Delta f_{A1}$$

(9)

Here the atom of interest is represented by $j = 1$ and Δf_{A1} is the difference between the complex anomalous scattering factors at the higher and lower energies. The change in the diffraction intensity is given by:

$$\Delta I(\vec{k}) = D(\rho_H, \vec{k}) - D(\rho_L, \vec{k}) . \tag{10}$$

Notice that the first term in Eq. 9 is determined directly from the COBRA analysis of the full data set measured at the lower energy, and $\rho_{i1}^A(\vec{r} - \vec{r}_i)$ is given by Eq. 5, so the only unknowns are the values of c_{i1}. These values can be determined by fitting the measured $\Delta I(\vec{k})$ with the values calculated using Eq. 10. In general we can fit the differential data on all symmetry inequivalent Bragg rods. Therefore the number of experimental data points is much larger than the number of occupancy parameters. In principle this allows us to determine all the occupancies

of the probe atom within one 2D folded unit cell. If the atomic species of interest can be assumed to be uniformly distributed within each monolayer, as is the case with our present samples, then the procedure is the same except the energy difference measurement needs to be done only along the (0,0,L) Bragg rod and c_{i1} then become the fractions of atomic species 1 in the i^{th} monolayer.

c. Determination of the complex Sr scattering cross-section

The atomic scattering cross-section at energies close to the absorption edge was determined experimentally using the Diffraction Anomalous Fine Structure (DAFS) method [18]. The diffraction intensity at one point along one of the Bragg rods ($\vec{k} = const$) is measured as a function of energy across the absorption edge. This spectrum can be expressed in terms of the probe scattering factor

$$\begin{aligned} I_d(E) &= A[1+\alpha(E-E_0)]\left|S_0 + S_f[f_{A1}^r(E) + if_{A1}^i(E)]\right|^2 \\ &= \overline{A}[1+\alpha(E-E_0)]\left|1 + \overline{S}_f[f_{A1}^r(E) + if_{A1}^i(E)]\right|^2 \end{aligned} \qquad (11)$$

Here, $\overline{A}$ and α are constants; α is small and corrects for small inaccuracies in detector and filter calibrations; S_0 is the complex scattering factor of the sample including the ordinary contribution of the probe but excluding the energy dependent part. So S_0 is a complex constant. S_f is the structure factor of the probe atoms at constant $\vec{k}$ so it is also a constant; f_{A1}^r and f_{A1}^i are the real and imaginary parts (the Kramers-Kronig, KK, conjugates) of the atom anomalous scattering factor.

KK conjugation requires integration over energy from 0 to infinity, while we have the data in a limited range of energies. So we calculated a correction function $f_c(E)$ defined as follows:

$$f_t^i(E) = \frac{-1}{\pi}\Pr\int_0^{\infty}\frac{2Ef_t^r(E')}{E'^2 - E^2}dE' = \frac{-1}{\pi}\Pr\int_{E_1}^{E_2}\frac{2Ef_t^r(E')}{E'^2 - E^2}dE' + f_c^i(E)$$
$$f_t^r(E) = \frac{1}{\pi}\Pr\int_0^{\infty}\frac{2E'f_t^i(E')}{E'^2 - E^2}dE' = \frac{1}{\pi}\Pr\int_{E_1}^{E_2}\frac{2E'f_t^i(E')}{E'^2 - E^2}dE' + f_c^r(E) \qquad (12)$$

f_t^r and f_t^i are the tabulated real and imaginary parts of the probe scattering cross-section. f_c^r and f_c^i are the integrals in the region outside the (E_1,E_2) range. So, changes in the probe environment that affect f_{A1}^r and f_{A1}^i at energies close to the absorption edge have a negligible effect on f_c^r and f_c^i.

We can now fit the calculated and experimental diffraction intensities $I_d(E)$ using the 4 parameters $\overline{A}$, α and the complex parameter $\overline{S}_f$ while the real and imaginary parts of $f(E)$ are allowed to change but are constrained to be the KK conjugates of each other and equal to the tabulated values when $|E - E_m| > 300eV$. To determine the change in the scattering cross-section of Sr near its absorption edge, we measured the diffraction intensity as a function of photon energy at $\vec{k} = [0\ 0\ 7.55]$. We chose this point because the diffraction has a maximum there, so it is large and only weakly dependent on $|\vec{k}|$. Thus any inaccuracies in the sample reorientation will introduce a negligible error. The measured diffraction intensity is shown in Fig. 2a. The

calculated complex scattering cross-section of Sr and the values obtained from X-ray tables are shown in Fig. 2b. Notice that indeed the new calculated complex scattering factor and the tabulated one agree when $|E - E_m| > 300eV$. The difference between the Sr complex anomalous scattering factor at the higher energy (16.08 keV) and lower energy (15.50 keV) was found to be $\Delta f_{A1} = -4.9 + 2.29i$.

III RESULTS AND DISCUSSIONS

The diffraction intensities of all three samples were measured along 10 symmetry-nonequivalent Bragg rods ranging from [00L] to [33L] using 15.50 keV photons. An example showing the diffraction intensity along the [00L] Bragg rod of sample S2 is shown in Fig. 3a. The data were analyzed using the COBRA method to obtain the approximate EDY. We then used the difference map method with the COBRA-derived EDY to obtain a more accurate EDY and a better fit to the experimental results [19]. An example of the fits is seen in Fig. 3a. The EDY of sample S2 along the [0 0 Z] line, perpendicular to the surface, is shown as an example in Fig. 3b. This line (line 1) goes through La/Sr, O, Al and Cu atoms. The atoms along the [0.5 0.5 Z] line (line 2) are displaced by 1/2 of the unit cell in the perpendicular direction (see the schematic of the structural model in Fig. 4), so each Cu atom along line 2 is located exactly midway between two La/Sr sites on line 1. Various atoms can be clearly identified. Notice that the La/Sr peaks above (to the right of) the Cu atoms along the line 2 are smaller than those below (to the left) suggesting that the Sr concentration in the layers immediately above the CuO_2 planes is larger than in those below.

We next used this EDY to obtain the normalized EDY's ρ^o and ρ^A at the La/Sr sites and, using the monolayer Sr concentrations c_{i1} as parameters, fitted the calculated differential diffraction intensity to the experimentally measured one. To obtain the information we need, i.e., the Sr concentration in each monolayer, it suffices to measure the differential diffraction just along the [00L] rod. The results are shown in Fig. 4. The best fit between the calculated and measured differential diffraction intensities is presented in Fig. 4a, and the fractional occupancy of Sr in each monolayer is shown in Fig. 4b. The uncertainty in the monolayer Sr occupancies, c_{i1}, was estimated using the Hessian distribution associated with the fit procedure; it was found to be ± 0.04.

As seen in Fig. 4a the differential diffraction signal is large only close to the Bragg peaks. This is to be expected because the change in the complex scattering factor resulting from the change in energy is small and the main contribution to the measured differential diffraction intensity is due to the mixed term involving the product of the scattering factor and the differential scattering factor. So to see more clearly the differential contribution we have plotted $\Delta I / \sqrt{I}$ in Fig. 4c. In this way the differential diffraction in the regions between the Bragg peaks have been magnified by as much as a factor of 100. In spite of this, the contributions are still small there and completely dominated by noise. In fact this tells us that the Sr density varies rather slowly from one unit cell to the next. The region with significant differential signal extends over approximately one third of the distance between the two symmetry allowed Bragg peaks. This means that in the present case, except for the up-down jumps which contribute to the differential diffraction intensity at all values of k, the measured Sr concentrations are averages over about 2 unit cells.

It is usually assumed, explicitly or implicitly, that in LSCO the Sr concentration is the same in each La/Sr layer. Under our synthesis conditions, Sr should definitely be able to diffuse a few atomic distances and then the entropy should favor random and uniform mixing. However, our study of the *M-I* bilayer (sample S1) shows that the EDY's at adjacent layers are very different, see Fig. 4b. The concentration of Sr in the layers just above the CuO_2 planes is much larger than in the layers below it. Attempts to fit the data with equal EDY's on adjacent La/Sr monolayers, or to reverse the order, failed completely.

In more detail, the first 16 atomic monolayers from left to right in Fig. 4b correspond to 4 $LaSrAlO_4$ unit cells; here the Sr concentration is uniform as expected. Sample S1 (see Fig. 4b) had 3 unit cells of metallic (M) $La_{1.55}Sr_{0.45}CuO_4$ and 3 unit cells of insulating (I) La_2CuO_4. In the metallic part, the Sr concentration is larger in every (L,Sr)O atomic layer that lies just above a CuO_2 layer and smaller in the (L,Sr)O atomic layer just below it. Above the nominal geometric $La_{1.55}Sr_{0.45}CuO_4/La_2CuO_4$ interface, the Sr concentration indeed falls off sharply. Nevertheless, a small amount of Sr has diffused into these insulating layers and even here one can discern a larger Sr concentration in the (La,Sr) monolayers just above the CuO_2 layers.

Since we found this result surprising, we decided to repeat these measurements on two additional samples with different and deliberately asymmetric growth sequences as described in the MBE synthesis section. The fits are shown in Fig. 5 and the EDY's are presented in Fig. 6. The results clearly show that the Sr concentration is again very different in adjacent monolayers. While this was expected, the surprise is that here again the layers with higher Sr concentration are the (La,Sr)O layers that lie just above the CuO_2 layers, in both cases – independent on where the Sr was placed originally. In finer detail, the Sr concentration in sample S3 is at first larger in

the layers below the Cu but then it also switches to the same sequence as observed in the other two samples.

As described in the MBE synthesis section, the deposition sequences of the three samples studied here were quite different. In sample S1, the growth sequence was programmed for Sr concentration nearly equal above and below the CuO_2 layers. In sample S2, all of Sr was deliberately deposited before the CuO_2 layer, while in sample S3 it was deposited after the CuO_2 layer. The fact that in samples S1 and S2 the experimentally observed structure differs from the programmed growth sequence means that under the present growth conditions Sr can indeed diffuse across a few atomic monolayers. This is also supported by the fact that some Sr is present in the insulating layers in sample S1.

On the other hand, the fact that Sr concentration alternates in adjacent (La,Sr)O layers suggests that this arrangement has a significantly lower free energy in spite of the decrease in entropy. Systematically much larger Sr concentration in the monolayer right above the CuO_2 layer implies that a symmetry-breaking interaction is at play. The growth sequence (kinetics) does not seem to be the key factor here because samples S2 and S3 with opposite growth sequences yielded the same result. Another apparent symmetry-breaking factor is the influence of the substrate, both geometric and electrostatic. Haskel *et al.* have shown that the La-apical oxygen distance is 2.35 Å and the Sr-apical oxygen distance 2.50 Å [23]. Hence, if a monolayer contains both La and Sr, the (La,Sr)O layer and/or its adjacent layers will likely be corrugated. Concentrating all the Sr into a single layer instead of spreading it between the two may reduce the corrugation and thus the elastic energy. However, this is not observed in bulk crystals, and it

would not explain the specific sequence of the Sr concentrations we observed here. Another aspect is electrostatics: Sr^{2+} has less charge than La^{3+}, and this substitution modifies the Madelung energy, which is poorly screened along the *c*-axis and long-ranged. Note that the sequence of charges in $LaSrAlO_4$ substrate layers, viz., $(La_{0.5}Sr_{0.5}O)^{+0.5}/(AlO_2)^{-1}/(La_{0.5}Sr_{0.5}O)^{+0.5}$, is very different from the one in La_2CuO_4, viz., $(LaO)^{+1}/(CuO_2)^{-2}/(LaO)^{+1}$. This causes electrostatic imbalance at the interface, which frequently leads to some local charge accumulation, the influence of which can propagate over many layers (the "Madelung strain") [24].

IV. SUMMARY

To conclude, we have developed a method to determine the concentration of an atomic species (the probe) in sites shared by two or more different species. The method consists of measuring the difference in the diffraction intensity at two different X-ray energies, one just below the absorption edge of the probe where the scattering cross-section has a minimum and another far enough in energy. Using the 3D EDY of the film determined by surface X-ray diffraction and analyzed by COBRA, we can calculate the differential diffraction in terms of the probe concentrations in each monolayer as parameters. Fitting the calculated differential diffraction to the experimentally measured one yields the probe concentration in each monolayer. To our surprise, we have found that in three LSCO films grown on $LaSrAlO_4$ substrates under different growth conditions the Sr concentration alternates from one La/Sr layer to the next. The concentration of Sr is systematically much lower in monolayers just below the CuO_2 layer and much larger in the La/Sr layer above it. This is true even in sample S2 where the film deposition kinetics explicitly favored the opposite concentration sequence.

This result means that, in contrast to the situation in the bulk samples, the inversion symmetry breaks down in MBE-grown films. Preliminary analysis of Ge quantum dots grown on Si suggest a similar effect indicating that such symmetry breaking may take place in many different thin films, and affect profoundly their optical and electronic properties. It is therefore important to unravel the cause of this phenomenon, to investigate how various parameters affect it, and how it can be used to engineer novel thin-film materials with desired properties.

ACKNOWLEDGEMENTS

I.B. and R.P. were supported by U.S. Department of Energy (DOE), Office of Basic Energy Sciences, Division of Materials Sciences and Engineering and Division of Scientific Users Facilities, respectively. Use of the Advanced Photon Source was supported by the U.S. DOE under Contract No. DE-AC02-06CH11357. Y.Y. was supported by the Israel Science Foundation grant No. 1005/11.

* To whom correspondence should be addressed at: 725D National Synchrotron Light Source, Brookhaven National Laboratory, Upton, New York 11973 U.S.A. E-mail: pindak@bnl.gov

[1] Blinc R (2011) Advanced Ferroelectricity. (Oxford University Press).

[2] S. W. Cheong, and M. Mostovoy, Nature Mater. **6**, 13 (2007).

[3] R. Ramesh, and N. A. Spaldin, Nature Mater. **6**, 21 (2007).

[4] N. A. Spaldin, M. Fiebig, and M. Mostovoy, J. Phys. Cond. Mat. **20**, 434203 (2008).

[5] L. P. Gor'kov, and E. I. Rashba, Phys. Rev. Lett. **87**, 037004 (2001).

[6] M. Z. Hasan, and C. L. Kane, Rev. Mod. Phys. **82**, 3045 (2010).

[7] A. Gozar, G. Logvenov, L. Fitting Kourkoutis, A. T. Bollinger, L. A. Giannuzzi, D. A. Muller, and I. Božović, Nature **455**, 782 (2008).

[8] G. Logvenov, A. Gozar, and I. Božović, Science **326**, 699 (2009).

[9] A. T. Bollinger, G. Dubuis, J. Yoon, D. Pavuna, J. Misewich, and I. Božović, Nature **472**, 458 (2011).

[10] A. Ohtomo, and H. Y. Hwang, Nature **427**, 423 (2004).

[11] N. Reyren, S. Thiel, A. D. Caviglia, L. Fitting Kourkoutis, G. Hammerl, C. Richter, C. W. Schneider, T. Kopp, A.-S. Rüetschi, D. Jaccard, M. Gabay, D. A. Muller, J.-M. Triscone, and J. Mannhart, Science **317**, 1196 (2007).

[12] A. V. Boris, Y. Matiks, E. Benckiser, A. Frano, P. Popovich, V. Hinkov, P. Wochner, M. Castro-Colin, E. Detemple, V. K. Malik, C. Bernhard, T. Prokscha, A. Suter, Z. Salman, E. Morenzoni, G. Cristiani, H.-U. Habermeier, and B. Keimer, Science **332**, 937 (2011).

[13] J. Chakhalian, J. W. Freeland, G. Srajer, J. Strempfer, G. Khaliullin, J. C. Cezar, T. Charlton, R. Dalgliesh, C. Bernhard, G. Cristiani, H.-U. Habermeier, and B. Keimer, Nature Physics **2**, 244 (2006).

[14] S. Smadici, J. C. T. Lee, S. Wang, P. Abbamonte, A. Gozar, G. Logvenov, C. D. Cavellin, and I. Božović, Phys. Rev. Letters **102**, 107004 (2009).

[15] I. Božović, IEEE Trans. Appl. Superconduct. **11**, 2686 (2001).

[16] D. P. Kumah, S. Shusterman, Y. Paltiel, Y. Yacoby, and R. Clarke, Nature Nanotechnology **4**, 835 (2009).

[17] C. Park, and P. A. Fenter, J. Appl. Crystallography **40**, 290 (2007).

[18] J. O. Cross, Analysis of diffraction anomalous fine structure. Ph.D. dissertation 1996, University of Washington, Seattle WA, USA.

[19] H. Zhou, Y. Yacoby, V. Y. Butko, G. Logvenov, I. Božović, and R. Pindak, Proc. Nat. Acad. Sci. **107**, 8103 (2010).

[20] V. Elser, Acta Crystallographica A **59**, 201 (2003).

[21] Y. Yacoby, R. Pindak, R. MacHarrie, L. Peiffer, L. Berman, and R. Clarke, J. Phys.: Condens. Matter **12**, 3929 (2000).

[22] International tables for X-ray crystallography, Vol. C pp 213-216. Dordrecht, D. Reidel 1983.

[23] D. Haskel, E. A. Stern, D. G. Hinks, A. W. Mitchell, and J. D. Jorgensen, Phys. Rev. B **56**, R521 (1997).

[24] V. Butko, G. Logvenov, N. Božović, Z. Radović, and I. Božović, Advanced Materials **21**, 3644 (2009).

Figure Legends

Figure 1. (Color online) Sample growth sequences. Schematic of the structure of three LSCO samples with nominal distribution of Sr dopant atoms as targeted by the atomic-layer deposition sequences. At room temperature, the structure is tetragonal and the space group is I4/mmm. The unit cell is delineated by the rectangular box. La: blue; Sr: green; Cu: red; Oxygen: yellow. ***a,*** LSCO with a random distribution of Sr atoms across the structure (as in the M layer in sample S1); ***b,*** LSCO with a preferential distribution of Sr atoms only below the CuO_2 plane (the sample S2); ***c,*** LSCO with a preferential distribution of Sr atoms only above the CuO_2 plane (the sample S3). The film growth direction is indicated by the arrow.

Figure 2. (Color online) The real and the imaginary parts of the Sr scattering cross-section. The complex scattering cross section of Sr was determined using the diffraction anomalous fine structure method. ***a,*** The anomalous diffraction intensity of the cuprate thin film measured at L=7.55 r.l.u.; ***b,*** The experimentally determined complex scattering cross-section of Sr as compared to the tabulated values.

Figure 3. (Color online) Bragg rod measurement, COBRA-determined electron density and fit. ***a,*** A representative example of the dependence of specular diffraction intensity on the momentum transfer along the (00L) Bragg rod measured on the single-layer metallic cuprate sample S2 (dots) and calculated from the COBRA-determined electron density (solid line). The arrow at L=7.55 reciprocal lattice units (r.l.u.) indicates the point at which the diffraction intensity was measured as a function of energy. ***b,*** The electron density along the [0 0 Z] line

through La/Sr, O, Al and Cu atoms. The topmost four unit cells of the substrate are included in the structure refinement. The dashed line represents the nominal substrate/metal interface. Cu(2) represents the positions of Cu atoms along the [0.5 0.5 Z] line.

Figure 4. (Color online) Differential Bragg rod data and the measured Sr concentration profile. The results are shown here for sample S1, a metallic-insulating (*M-I*) bilayer film. ***a,*** The measured differential energy data for the (00L) Bragg rod, and the fit using the method described in the text. ***b,*** The Sr occupancy at the A-site in the lattice across the *M-I* bilayer system. The topmost four unit cells of the substrate are included in the refinement. The positions of respective CuO_2 planes in each unit cell are marked by the short bars. The vertical dashed and dotted lines represent the nominal substrate/metal and metal/insulator interfaces, respectively. The horizontal long dashed and dotted lines represent the nominal Sr site occupancies inside the substrate (0.5) and metal layers (0.22), respectively. A planar projection of the structural model is included where line (1) indicates the row of atoms along the [0 0 Z] line while line (2) indicates the row of atoms along the [0.5 0.5 Z] line with La/Sr: blue; Cu: red; Oxygen: yellow. ***c,*** The measured relative differential energy data for the (00L) Bragg rod, and the fit described in the text.

Figure 5. (Color online) Differential Bragg rod (00L) measurements and fits. The results are shown for ***a,*** sample S2 and ***b,*** sample S3.

Figure 6. (Color online) The Sr site occupancies determined by the differential method for the two metallic single-layer films with the same nominal composition but different growth conditions. ***a,*** sample S2 and ***b,*** sample S3. The positions of respective CuO_2 planes in each unit

cell are marked by the short bars. The vertical dashed line represents the nominal substrate/metal interface. The horizontal long dashed and dotted lines represent the nominal Sr site occupancies inside the substrate (0.5) and metal layers (0.22), respectively.

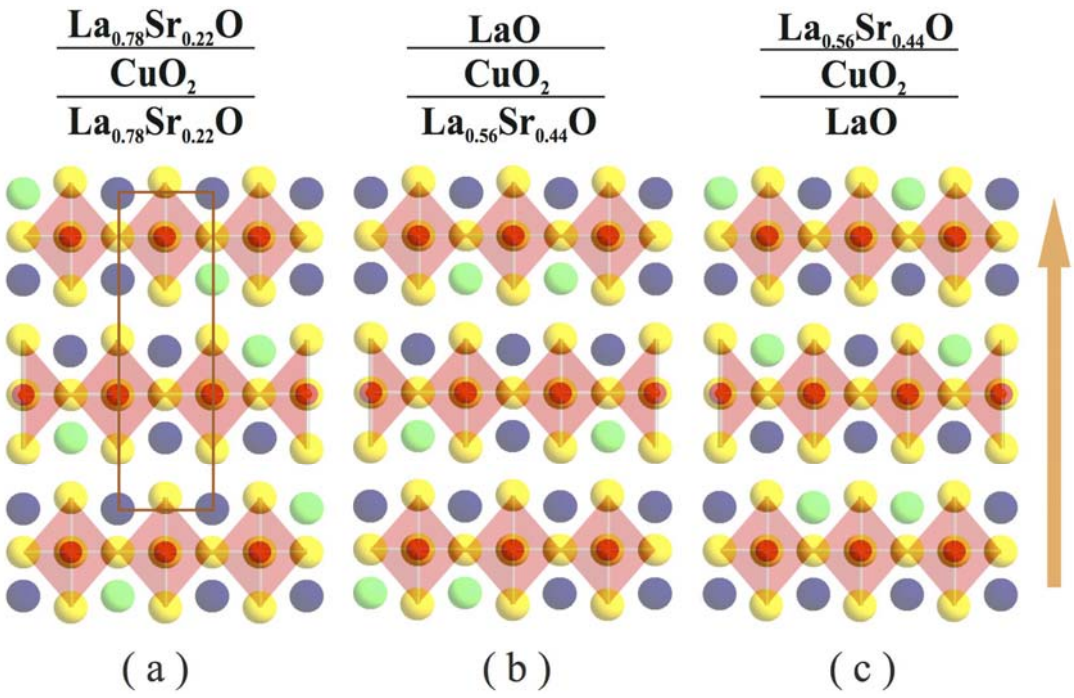
$La_{0.78}Sr_{0.22}O$
CuO_2
$La_{0.78}Sr_{0.22}O$
LaO
CuO_2
$La_{0.56}Sr_{0.44}O$
$La_{0.56}Sr_{0.44}O$
CuO_2
LaO
(a)
(b)
(c)

Figure 1

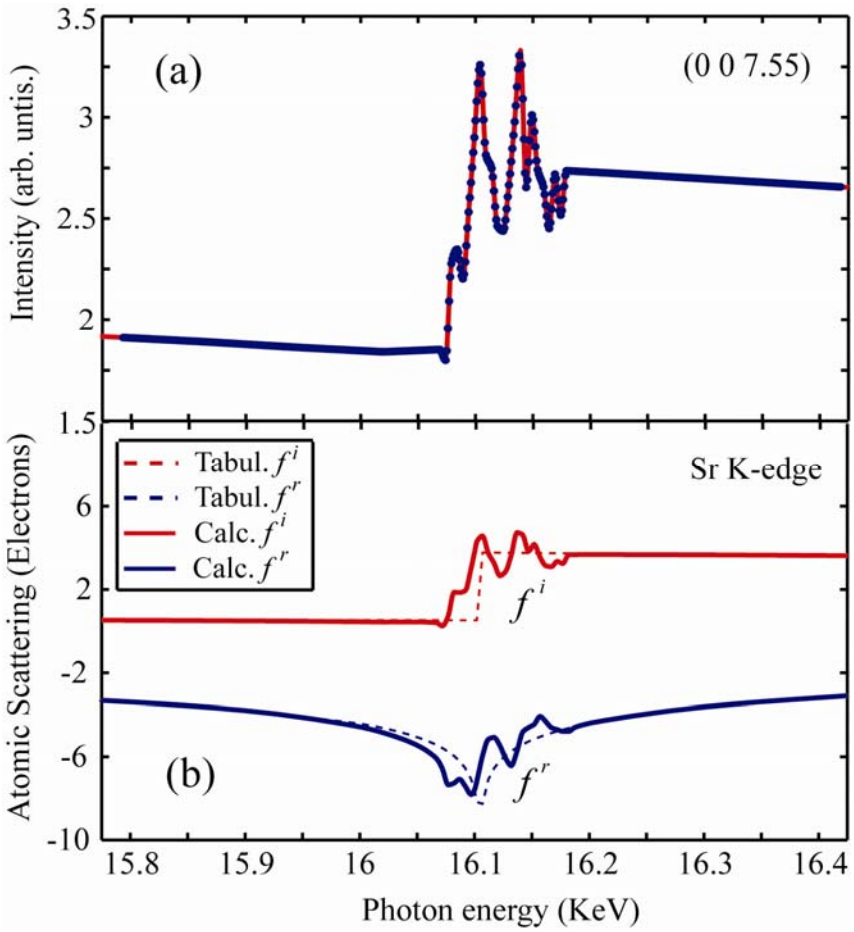
(a)
(0 0 7.55)
Intensity (arb. untis.)
3.5
3
2.5
2
1.5
(b)
Sr K-edge
Tabul. f^i
Tabul. f^r
Calc. f^i
Calc. f^r
f^i
f^r
Atomic Scattering (Electrons)
6
2
-2
-6
-10
15.8
15.9
16
16.1
16.2
16.3
16.4
Photon energy (KeV)

Figure 2

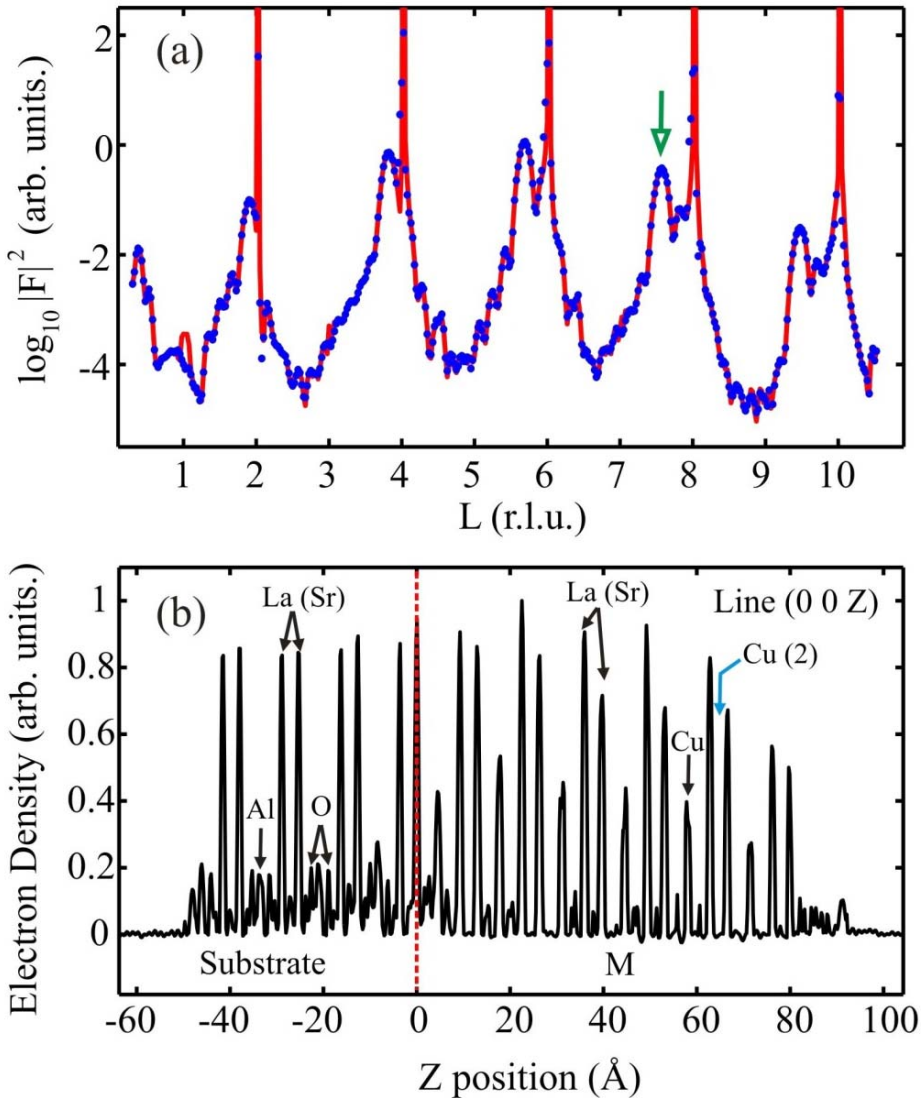
(a)
$\log_{10}|F|^2$ (arb. units.)
L (r.l.u.)
(b)
La (Sr)
La (Sr)
Line (0 0 Z)
Cu (2)
Cu
Al
O
Substrate
M
Electron Density (arb. units.)
Z position (Å)

Figure 3

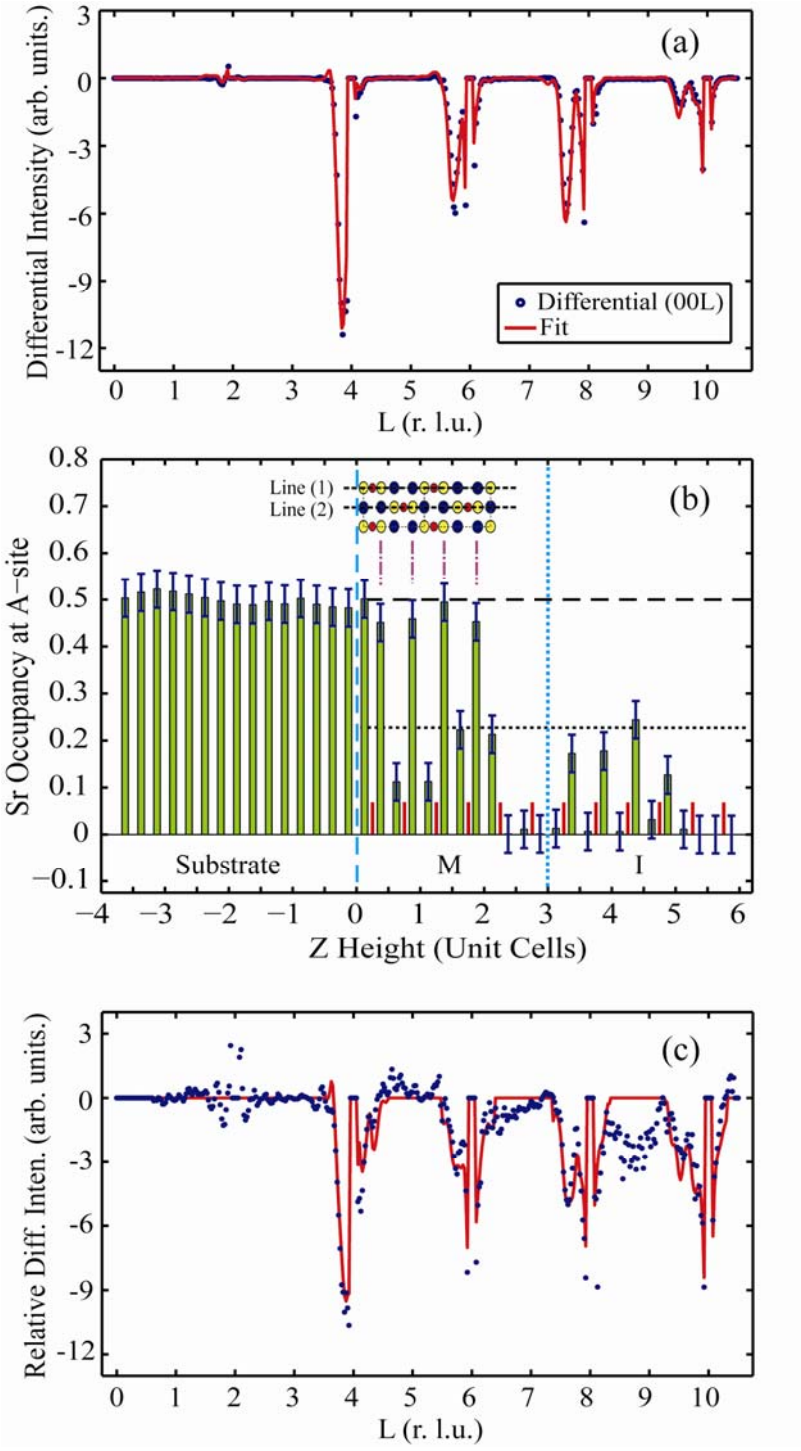
(a)
Differential Intensity (arb. units.)
Differential (00L)
Fit
L (r. l.u.)
(b)
Line (1)
Line (2)
Sr Occupancy at A−site
Substrate
M
I
Z Height (Unit Cells)
(c)
Relative Diff. Inten. (arb. units.)
L (r. l.u.)

Figure 4

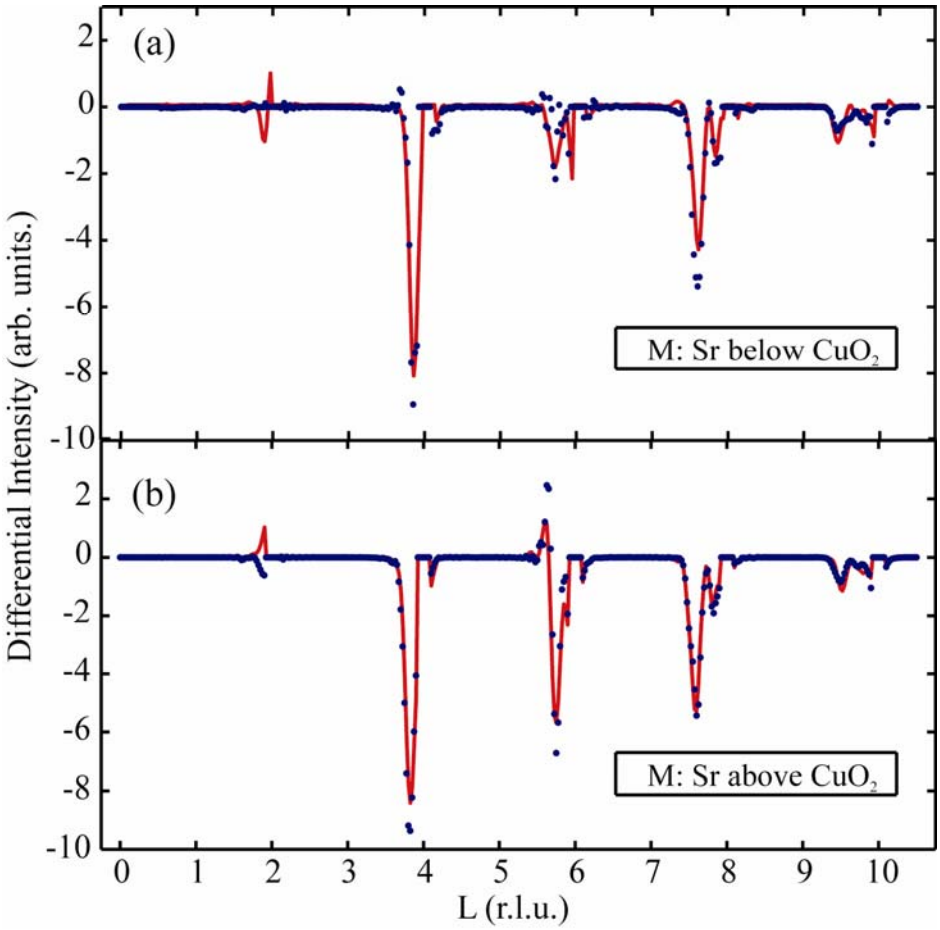
(a)
(b)
M: Sr below CuO_2
M: Sr above CuO_2
Differential Intensity (arb. units.)
L (r.l.u.)
2
0
-2
-4
-6
-8
-10
0
1
2
3
4
5
6
7
8
9
10

Figure 5

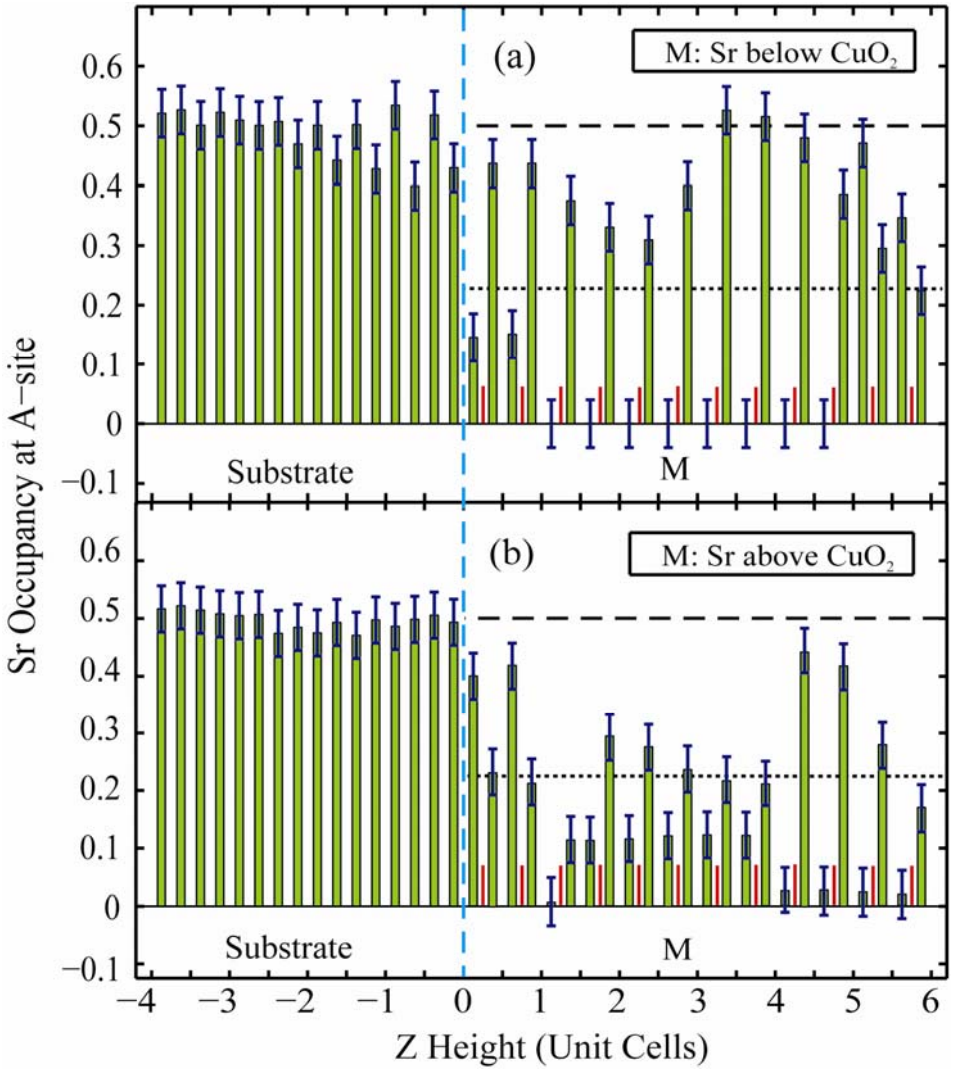
(a)
M: Sr below CuO_2
(b)
M: Sr above CuO_2
Substrate
M
Sr Occupancy at A−site
Z Height (Unit Cells)
0.6
0.5
0.4
0.3
0.2
0.1
0
−0.1
−4
−3
−2
−1
0
1
2
3
4
5
6

Figure 6